IEEE Access
Multidisciplinary | Rapid Review | Open Access Journal

Received 31 May 2022, accepted 28 June 2022, date of publication 4 July 2022, date of current version 12 July 2022.

Digital Object Identifier 10.1109/ACCESS.2022.3188455

RESEARCH ARTICLE

The B-Scan Image Simulation Method of a Ground-Penetrating Radar Mounted on a Drone Using a High-Frequency Technique

KITTISAK PHAEBUA[1], (Member, IEEE), TITIPONG LERTWIRIYAPRAPA[1], (Senior Member, IEEE), SANTANA BURINTRAMART[2], AND AKKARAT BOONPOONGA[3], (Member, IEEE)

[1]Research Center of Innovation Digital and Electromagnetic Technology (iDEMT), Department of Teacher Training in Electrical Engineering, Faculty of Technical Education, King Mongkut's University of Technology North Bangkok, Bangkok 10800, Thailand
[2]Magpie Patent and Technology Company Ltd., Ban Mai, Pakkret, Nonthaburi 11120, Thailand
[3]Department of Electrical and Computer Engineering, Faculty of Engineering, King Mongkut's University of Technology North Bangkok, Bangkok 10800, Thailand

Corresponding author: Akkarat Boonpoonga (akkarat.b@eng.kmutnb.ac.th)

This work was supported in part by the King Mongkut's University of Technology North Bangkok under Grant KMUTNB-64-KNOW-29, and in part by the Air Force Office of Scientific Research under Award FA2386-19-1-4035.

ABSTRACT A B-scan image simulation method of a ground-penetrating radar mounted on a drone using a high-frequency technique is proposed. The proposed simulation method aims to predict drone mounted-GPR receiving signals in a complex three-dimensional (3D) scenario, including the reflected signal from various ground types, backscattered signals from considered underground objects, and backscattered volume clutter signals from underground random object clusters. The modeled scenario, including various 3D drone trajectories, target objects, underground random object clusters, ground types, antenna radiation patterns, and desired transmitting time-domain short pulse signals, are taken into account. A high-frequency technique consisting of the geometrical optic (GO) ray-tracing technique to find the GO ray paths, and the GO ray field approximation technique to find the electromagnetic (EM) fields of every GO ray path, are employed instead of conventional numerical methods. This is useful for EM problems with large computational domains. The efficiency in terms of computational time and computer resources is better than that of numerical techniques. Finally, the effect of drone positioning errors, ground types, underground random object clusters, and the antenna radiation patterns on A-scan and B-scan images of adrone-mounted GPR will be illustrated. It is found that the distortion of the hyperbolic signature of underground target objects in the B-scan image occurred by unwanted back-scattered signals or radar clutter from the ground surface, volume clutter from underground random object clusters, and drone positioning errors. Moreover, a high directivity antenna enhances the intensity of the hyperbolic signature. The proposed simulation method will be useful for predicting the drone mounted-GPR signals in various complex 3D scenarios, having various kinds of transmitting signals, and target object configurations and antenna types.

INDEX TERMS Ground-penetrating radar, GPR mounted on drone, B-scan image simulation method, geometrical optic (GO), ray-tracing technique.

I. INTRODUCTION

A short pulse radar, namely time-domain (TD) ground-penetrating radar (GPR), employs an electromagnetic wave to detect underground objects by sensing a backscattered wave. The TD-GPR has been widely employed in many applications [1]–[3]. Examples of GPR applications such as agriculture and forestry applications for sensing water and moisture under the ground, archaeology for locating foundations, concrete structures underneath the ground, oil and gas explorations, and mining and others were presented in [1]–[5]. Moreover, conventional handheld GPR and

The associate editor coordinating the review of this manuscript and approving it for publication was Santi C. Pavone.

GPR mounted on a car are employed in various military applications [3]–[5], especially for the detection of an improvised explosive device (IED), which can be installed in gas tanks and embedded under the ground [4], [5]. The experimental study of car-mounted GPR for improvised-explosive device detection in Thailand was proposed in [4]. The experiment found that the proposed regionalization and hyperbolic or palabolic identification (signature) techniques were successfully employed [4]. Moreover, an automatic detection and classification technique of objects buried under the ground was proposed [5]. Car-mounted GPR signal post-processing techniques have been proposed to increase detection performance, consisting of ground surface clutter reduction, the estimation of late-time response, pole extraction, and object classification techniques [5].

However, the operation of handheld GPR and conventional car-mounted GPR is very slow and is not suitable for some military applications, such as underground IED detection for military convoys. Normally, a military convoy travels at a speed much faster than the speed at which an IED detection system can detect an IED. Thus, an early warning system (EWS) must be able to detect an IED a few seconds before the military convoy passes the IED point. In order to reduce the damage to the vehicle, injury, and losses of lives, a GPR mounted on a drone is very challenging. Unmanned aerial vehicle (UAV) -based GPR technology has been developed [3]–[11]. This can be categorized according to two types of GPR. First, on-ground GPR mounted on a car system has been proposed in [3]–[6]. In [6], the UAV-mounted GPR is located above a ground of 0.5 meter. It is considered as nearly near-field scenarios. The simulation result was carried out by a simple model of gprMax simulation software. Two PEC cylinders were employed as the buried objects. However, the effect of underground clutter radar signal (backscattered signal) from underground random object clusters is not included. The effect of the constructive and destructive interferences on the receiving GPR signals from multi-path rays of the underground small scattering objects which represent the underground small stone and gravel is not included as well. Second, above-ground GPR mounted on a drone system is proposed in [7]–[11]. The GPR mounted on a drone can be autonomously flown to detect considered objects for various applications. B-scan drone mounted-GPR images of the mortar grenade underground were investigated, as shown in [7]. Additionally, a synthetic aperture radar imaging system for landmine detection using ground-penetrating radar onboard an unmanned aerial vehicle was presented in [8]. Airborne multi-channel ground-penetrating radar for improvised explosive devices and landmine detection was proposed in [9], and low-altitude autonomous drone navigation for landmine detection purposes was presented in [10]. In the experimental studies seen in [7]–[9], low transmitted power and the ground loss affect the hyperbolic signature intensity. The drone mounted-GPR system was controlled to be around 1 to 2 meters in height in order to increase the hyperbolic signature intensity. In order to reduce the effect of the electromagnetic (EM) wave scattered from the small stone and gravel underneath the ground on the hyperbolic signature intensity, the drone mounted-GPR system should be operated at a low attitude. However, the altitude of the airborne GPR employed to explore the groundwater was investigated up to 1000 meters [11]. It was found that the survey altitude, survey area, antenna beam, transmitted power, and the frequency bandwidth of the GPR result in the received signal strength directly associated with the hyperbolic signature. The GPR operation at a very high altitude is therefore challenging. The use of a drone carrying the GPR is more time efficient than that of a conventional car-mounted GPR system. Indeed, the controlled altitude is usually chosen depending on the specific application of the GPR. The previous works in [7]–[11] are based on experimental procedures. 3D complex scenario simulations and analysis were omited. In addition, unwanted signals or radar clutters such as reflections from the ground surface, radar clutter signals from the soil, and underground objects (small stone and gravel) are not well studied. These parameters affect the detection performance of the drone mounted-GPR system. Currently, many post-processing algorithms are proposed to improve car-mounted GPR images by eliminating ground reflection and soil clutter signals from the total GPR signals [5]–[11]. The performance of algorithms were investigated by using a simple simulation method and EM propagation modeling [12]. Non-iterative techniques for GPR imaging through a nonplanar air-ground interface were presented in [12]. The spatial Fourier transform technique and finite-difference time-domain (FDTD) method to determine scattering EM fields and B-scan images were employed. However, soil volume clutter signal, underground clutter signal (small stone and gravel) prediction and three-dimensional (3D) drone mounted-GPR scenarios were not supported.

Furthermore, the computational domain size and computational time of the FDTD method are not efficient compared to high-frequency techniques [13] (analytical models) such as the geometrical optic ray (GO), the uniform geometrical theory of diffraction (UTD), and others. High-frequency techniques have been employed to calculate EM wave propagation [13]. The application of high frequency techniques for antenna analysis has been proposed in [14]. These techniques provide physical insight into antenna radiation mechanisms. It was found that antenna radiation mechanisms of various practical antenna configurations located on large platforms can be highly efficiently predicted [14]. Moreover, the path-loss prediction of radio wave propagation in an orchard by using the modified UTD method has been proposed [15]. The multiple rays of EM wave scattering from trees were included [15]. An overview of the electromagnetic simulation-based channel modeling techniques for wireless body area network applications have been proposed [16]. The channel modeling and simulation using electromagnetic based techniques such as high-frequency ray-tracing, UTD,

MoM, FEM, FDTD, and FIT-based channel modeling techniques are compared [16]. It was found that high-frequency ray-tracing and UTD are suitable for indoor and outdoor propagation prediction and large problems. Therefore, simple high-frequency ray-tracing has been employed for radar application, especially with GPR applications [17]–[20]. The synthetic aperture radar (SAR) target image simulation method with embedded deep neural network (DNN) to calculate electromagnetic reflection was proposed in [17]. The ray-tracing technique was employed to determine the radar cross-section (RCS) of an object. The hyperbolic summation method to focus B-scan ground-penetrating radar images with an experimental study of a stepped frequency system was presented in [18]. The physical optics (PO)-based and the shooting and bouncing ray (SBR) technique are employed. The simulation and measurement results were in good agreement. A study of the time-domain drone mounted-GPR prediction by using the UTD method was proposed in [19]. The drone mounted-GPR A-scan signal was calculated by using the ray tracing technique and UTD method. It was found that time-domain GPR signals such as ground reflections, object reflections, and object diffractions can be separately calculated. The signal delay time depends on the ray paths. Moreover, the drone mounted-GPR B-scan image prediction was proposed in [20]. It was observed that the hyperbolic signatures of underground objects and also the layers of the ground were illustrated in the B-scan image. Moreover, an algorithm for detecting subsurface voids under the road from ground penetrating radar images was proposed in [21]. The two-dimensional (2D) finite difference time domain (FDTD) method was employed. Hyperboloid reflection patterns of voids were extracted. 3D convolutional neural network (3D-CNN) and modeling GPR radar for subsurface analysis were presented in [22]. It is demonstrated that the target response can be obtained through FDTD-simulations and subsequent corrections. However, multi-layers with different permittivity were employed in order to easily represent practical situations. Moreover, according to the work in the literature [4]–[12] and [17]–[22], underground volume clutter radar signal modeling, antenna radiation patterns, and 3D drone mounted-GPR scenarios were not taken into account. The study of the positioning error of a drone trajectory was omitted, and the various kinds of soil types were not well studied.

This paper proposes a B-Scan image simulation method of a GPR mounted on a drone by using high-frequency techniques. A scenario modeling GPR mounted on a drone is shown in Fig. 1, where the transmitting (Tx) and receiving (Rx) antennas are installed on the drone. This is considered a far-field scenario. In the practical situations of Thailand's southern insurgencies, IEDs are installed with a gas tank and embedded under the road [4]–[5]. The actual environment can be modeled using canonical shapes, and then EM field strength can be predicted. The underground small stone and gravel mostly used to construct the road (compacted gravel road) were therefore represented by

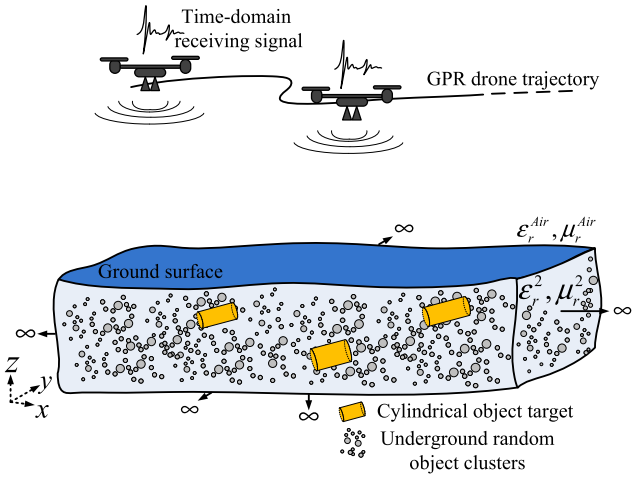

FIGURE 1. Scenario modeling of a GPR mounted on drone.

underground small scattered objects, as shown in Fig. 1. The main contributions of the proposed simulation method are as follows. First, the combination of a high-frequency technique [15], [23]–[24], based on field strength calculation, and the geometrical ray tracing technique employed to predict drone-mounted GPR receiving signals in a large and complex three-dimensional (3D) scenario, is proposed. Second, the effect of the constructive and destructive interferences on the receiving GPR signals from multi-path rays of the small underground scattered objects, which represent the underground small stone and gravel, is taken into account by using a high-frequency technique. The GPR signal attenuation and fading caused by underground radar clutters are considered as well. Third, hybrid simulations dealing with the proposed high-frequency and geometrical ray tracing techniques, along with an antenna radiation pattern simulated by commercial software [25], are introduced in order to improve the efficiency of the GPR simulation. The effects of various parameters, including drone positioning errors, ground types, underground targets, underground random object clusters, operating frequency, bandwidth, and the antenna radiation patterns on the B-scan GPR images were investigated via our simulations. In this paper, the slight roughness of a compacted gravel road will be assumed to be a smooth surface. Normally, slight surface roughness slightly affects the EM scattering. A rule of thumb for the smooth surface in microwave applications is that the roughness should be less than or equal to 0.1λ [26]–[27]. Also, possible interference due to drone equipment engines with devices is omitted. The radar payload, computational resources, and a suitable protocol are not included in this study.

The advantage of the simulation for a large and complex 3D scenario is its ability to predict and study the EM propagation channel characteristics; namely, the field strength everywhere in a considered area without having experiments using a real system or actual scenarios. The proposed simulation method will be useful for predicting the drone-mounted GPR signals in various complex 3D scenarios,

having various kinds of transmitting signals, underground objects, soil dielectric materials, target object configurations, and antenna types without having to experiment on the real system. In addition, commercial software based on conventional numerical methods, such as FDTD, MOM, FIT, and others, cannot be efficiently calculated due to the large computational domain (computer resources and computational time).

UTD solutions for EM waves scattered from curved surfaces are widely employed in many propagation problems such as in [13]–[16]. Here, the frequency-domain UTD is employed in order to compute the frequency spectrum of each channel, namely the channel transfer function ($H(j\omega)$) of incident, and the reflected and diffracted waves of the receiving antenna. The electromagnetic wave from a Tx antenna travels through the propagation channel, including air (free-space), the ground surface, underground random object clusters, and the underground target object, as shown in Fig.1. The modeled scenario includes a 3D drone trajectory, various target objects, underground random object clusters, various ground types, the antenna radiation pattern, and the desired transmitting time-domain short pulse signal.

II. THEORETICAL APPROACH

A. CONCEPT OF THE PROPOSED METHOD OF THE GPR MOUNTED ON DRONE

The total time-domain GPR pulse signal of each receiving position ($y_{Rx}(x, y, z, t)$) in (1) consists of signal distortion and time delay. It depends on the propagation channel and the RF equipment characteristics [2], [3] and [21], [22]. The RF equipment generates some signal distortion due to the imperfection of the frequency response characteristics. The data from the signal distortion from Tx and Rx antennas and RF equipments can be obtained by using simulation and measurement procedures. However, the signal distortions from antennas and the RF equipment are neglected in this paper in order to simplify the problem. Thus, the total time-domain GPR signal ($y_{Rx}(t)$) of each propagation channel of the n-channel at each receiver location ($P(x, y, z)$) can be obtained via a principle of the superposition of the EM waves travelling through the same medium at the same time as

$$y_{Rx}(t) = y^1_{Rx}(t) + y^2_{Rx}(t) \ldots + y^N_{Rx}(t) = \sum_{n=1}^{N} x_{Tx}(t) \otimes h^n_{Ch.}(t) \tag{1}$$

where $x_{Tx}(t)$ denotes the time-domain pulse signal from the Tx antenna. $h^n_{Ch.}(t)$ denotes the impulse response of the propagation channel (n), which is dependent on free-space loss, soil properties, and the underground scattering objects of each dominate GO ray path. N denotes the total number of the multiple propagation channels. Generally, the relation between time and frequency convolution can be written as

$$\begin{aligned} y^n_{Rx}(t) &= x^n_{Tx}(t) \otimes h^n_{Ch.}(t) \overset{FFT}{\underset{iFFT}{\Leftrightarrow}} Y^n_{Rx}(j\omega) \\ &= X^n_{Tx}(j\omega) \cdot H^n_{Ch.}(j\omega) \end{aligned} \tag{2}$$

where $H^n(j\omega)$ denotes the frequency transfer function of each n-channel, which is easily obtained by using high frequency methods such as UTD, physical optic (PO), the GO ray field method, and others. $X(j\omega)$ can be calculated by using a fast Fourier transform (FFT) algorithm. The time-domain drone mounted-GPR signal ($y^n_{Rx}(t)$) at each receiving location can be calculated by using an inversion fast Fourier transform (iFFT) as in (2). Using the high frequency method, the time-domain drone mounted-GPR signals of ground reflection, object reflection, and object diffraction can be separately calculated. Moreover, antenna characteristics are normally measured or simulated in the frequency-domain rather than in the time-domain such as a radiation pattern, gain and scattering parameter (S-parameters).

Finally, using the linearity properties of Fourier transform, the total time-domain GPR signal ($y_{Rx}(t)$) from the whole propagation channel of the n-channel at each receiver location ($P(x, y, z)$) can be written as

$$y_{Rx}(t) = \sum_{n=1}^{N} iFFT\left\{X_{Tx}(j\omega) \cdot H^n_{Ch.}(j\omega)\right\} \tag{3}$$

The computational procedure flowchart of the proposed method is shown in Fig. 2. The proposed procedure is as follows.

In step 1, the input data such as the drone trajectory, the cylinder target object location and antenna pattern, are imported.

In step 2, random object clusters (represented by small spheres), Gaussian monopulse, and ground types are defined.

In step 3, GO ray tracing to determine the GO ray path is performed.

In step 4, the radar cross-sections (RCS) of the objects and volume clutter signals are calculated. The GO ray path-loss and phase delay due to each GO ray path propagation channel are calculated. In this step, the frequency-domain transfer functions of each propagation channel are obtained.

In step 5, the backscattered waves (signals) of each drone mounted-GPR location from each propagation channel are calculated by using an iFFT algorithm to obtain the time-domain receiving signal.

Finally in step 6, the modeling scenario such as drone mounted GPR, object, clusters locations, GO ray paths, antenna radiation pattern, A-scan GPR signal, and B-scan GPR image is illustrated.

The time-domain transmitting signal data can be imported from measurement, mathematic solution, or simulation results. In this paper, a time-domain Gaussian monopulse is employed to represent the GPR transmitting signal. The Gaussian monopulse is written as

$$x_{Tx}(t) = V_0 e^{1/2}\left(\frac{t}{\rho}\right) e^{-\left(\frac{t}{\rho}\right)^2/2}, \tag{4}$$

where $\rho = 1/(2\pi f_c)$ and f_c denote the center frequency. The $V_0 = 1$ volt and t represent the signal peak voltage and time, respectively.

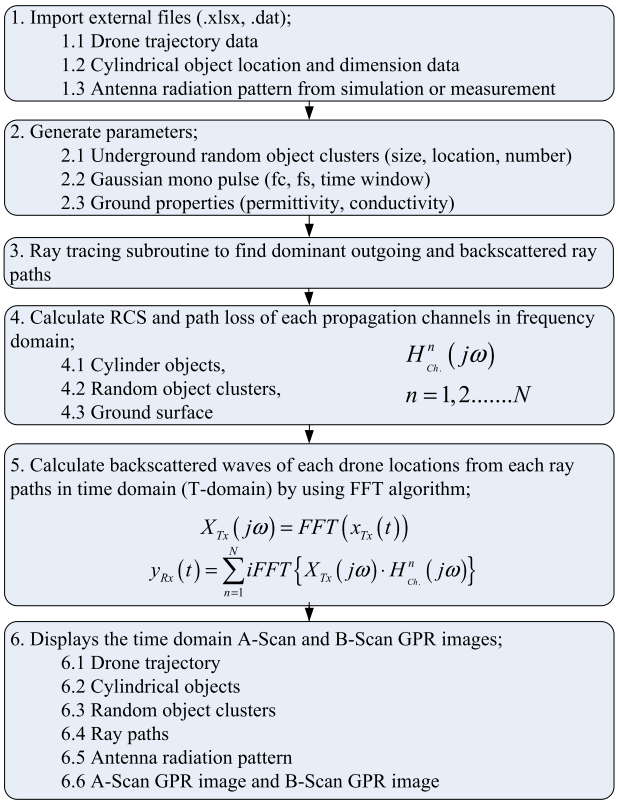

FIGURE 2. Flowchart of the proposed simulation method of a GPR mounted on a drone using a high-frequency technique.

The frequency-domain transfer function of each n-channel $H^n_{Ch.}(j\omega)$ can be calculated by using the high frequency technique. It is found that the incident and reflected ray field solution of the UTD is the same as the GO ray field solution that is employed in this paper. The incident and reflected frequency-domain UTD solution is adapted in order to compute the frequency spectrum or so-called channel transfer functions $H^n_{Ch.}(j\omega)$ of an incident, and the reflected and diffracted waves at the receiving antenna, which are radiated from the Tx antenna. The electromagnetic wave from the Tx antenna is passed through the propagation channel, including the air (free-space), soil, and underground, as shown in Fig.3. Thus, the distortion of the time-domain GPR signal depends on the delay and channel characteristic of each GO ray path.

Generally, the GO ray term in the UTD solution is expressed in the frequency domain. The approximated incident GO ray field ($E^i(P)$) at point P [15] can be written as

$$\bar{E}^i(P) \approx \bar{E}_0 \frac{e^{-jks^i}}{s^i}, \tag{5}$$

where $\bar{E}_0$ denotes the EM field complex amplitude of a spherical wave that is generated from the Tx antenna, including antenna gain, radiation pattern ($F_{ANT.}(\theta, \phi)$), and polarization and transmitting power (P_T); and s^i denotes the distance from the Tx source point to the considered point

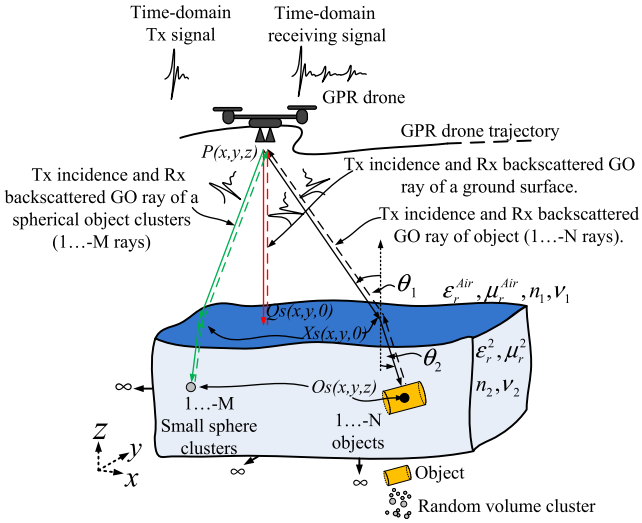

FIGURE 3. The concept of the ray tracing of a GPR mounted on a drone.

(P), such as the observation point, the ground reflection point (Q_s), the refraction point (X_s), and the object target scattering points (O_s). The magnitude of $\bar{E}^i(Q_s, X_s, O_s)$ is inversely proportional to frequency ($\approx 1/k$). The propagation path-loss (free-space loss) is inversely proportional to distance s^i. Thus, the approximated total GO ray field of the reflected wave from the ground surface ($\bar{E}^t_{Surface}$) at the receiving point (P) can be expressed as

$$\bar{E}^t_{Surface}(P) \approx \bar{E}^i(P) + \bar{E}^i(Q_s) \cdot \bar{\bar{R}} \cdot A \cdot e^{-jks^r} \tag{6}$$

and

$$A = \sqrt{\frac{\rho_1^r \rho_2^r}{(\rho_1^r + s^r)(\rho_2^r + s^r)}} \tag{7}$$

where $\bar{\bar{R}} = R_s \hat{e}_\perp \hat{e}_\perp + R_h \hat{e}^i_{||} \hat{e}^r_{||}$ represents the dyadic reflection coefficients, including $R_s = \Gamma_\perp$ acoustic soft (electric field perpendicular to the plan of incident) and $R_h = \Gamma_{||}$ hard (electric field parallel to the plan of incident) reflection coefficients. A and s^r represent the spreading factor of the reflected ray and the distance from the reflection point to the receiving point, respectively. In the case of a flat ground surface, the principal radii of the curvature (ρ_1^r, ρ_2^r) became $\rho_1^r, \rho_2^r \rightarrow s^i$. Moreover, in the case of monostatic radar configuration, the unidirectional pattern Tx and Rx antennas are located at the same location and are pointed to the ground. The Tx and Rx antennas coupling is very low due to low side-lobe levels. Thus, the coupling GO ray field of $\bar{E}^i(P) \approx 0$. In this paper, the polarization of the antenna is linearly polarized in the y-direction, which is parallel to the ground and approximately perpendicular to the plan of incident. Thus, the $R_s = \Gamma_\perp$ acoustic soft reflection coefficient is chosen to be the dominate polarization component and the cross-polarization is ignored. Therefore, the total reflected GO ray field from the ground surface in (6)

can be simplified as

$$E^{t}_{Surface}\left(P\right) \approx E_0 \cdot \Gamma_{\perp} \cdot \frac{e^{-jk\left(s^i+s^r\right)}}{\left(s^i+s^r\right)} \tag{8}$$

The reflection coefficient of the ground and air interface [23], [24] can be written as

$$\Gamma_{||,\perp} = \frac{\cos(\theta) - Z}{\cos(\theta) + Z} \tag{9}$$

where $Z = \sqrt{\varepsilon_r - jX - \sin^2(\theta)}/(\varepsilon_r - jX)$ for $\Gamma_{||}$ vertical polarization and $Z = \sqrt{\varepsilon_r - jX - \sin^2(\theta)}$ for $\Gamma_{\perp}$ horizontal polarization where $X = \sigma/\omega\varepsilon_0$.

Conventionally, the backscattered power density from the object at the receiver $P^s(P)$ in free space can be expressed as

$$P^s(P) = \sigma P^i(O_s) \tag{10}$$

The σ denotes the GO radar cross-section (RCS) in terms of power density. The RCS of the object is defined by the power density of the backscattered wave ($P^s(P)$) divided by the power density of the incident wave at the object location ($P^i(O_s)$). The scalar RCS of the object is written as

$$\sigma = \lim_{P\to\infty}\left[4\pi P^2 \frac{|E^s(P)|^2}{\left|E^i(O_s)\right|^2}\right], \tag{11}$$

where $E^s(P)$ and $E^i(O_s)$ are the scattered electric field and incident electric field intensities at far-field region, respectively. However, the GO RCS in terms of the EM field can be approximately calculated by $\sigma^{\text{GO field}}_{Object} \approx \sqrt{\sigma}$. Using the same procedure as in (8), the total backscattered GO ray field from the object underground can be constructed as

$$E^{t}_{Object}\left(P\right) \approx E_0 \cdot \sigma^{\text{GO field}}_{Object} \cdot \mathrm{T}_{21}\mathrm{T}_{12} \cdot \frac{e^{-jk(s_{Air})}e^{-(\alpha+j\beta)(s_{Soil})}}{(s_{Air}+s_{Soil})} \tag{12}$$

where $s_{Air} = s^i_{Air} + s^s_{\text{Air}}$ represents the incident path length and the backscattered GO ray path length in the air, and $s_{Soil} = s^i_{Soil} + s^s_{Soil}$ represents the effective length of the incident and backscattered GO ray path inside the soil, respectively. The i and s denote the incident GO ray and backscattered GO ray, respectively. Conventionally, the EM wave is propagated through the ground and air interface (refraction). The ohmic or material loss attenuation α is taken into account, as in (12). The cylindrical objects (target) create the dominant scattered fields. The $\alpha \approx (\sigma_{Cond.}/2)\sqrt{\mu/\varepsilon}$ and $\beta \approx \omega\sqrt{\mu\varepsilon}$ represent the attenuation and propagation constants of the GO ray field traveling inside the soil. The $\sigma^{\text{GO field}}_{Object} \approx \sqrt{\sigma}$ denotes the RCS of the objects, which depend on object configurations. $\mathrm{T}_{21} = 1 + \Gamma_{\perp}$ and $\mathrm{T}_{12} = 1 + \Gamma'_{\perp}$ denote the transmission coefficients of the GO ray field traveling from the air to underground (T_{21}) and the GO ray field traveling from the underground layer to the air (T_{12}), respectively. In the situation of a single backscattered GO ray, the $\mathrm{T}_{21} \approx \mathrm{T}_{12}$ is effectively employed. It satisfies the reciprocal property of the EM wave traveling forth and back at the air and ground interface. Finally, the frequency transfer function of each propagation n-channel can be expressed as

$$H^{n}_{Ch.}\left(j\omega\right) \approx \begin{cases} E^{t}_{Surface}\left(P, j\omega\right), & \text{for} n = 1 \\ E^{t,n}_{Object}\left(P, j\omega\right), & \text{for} n > 1 \end{cases} \tag{13}$$

where $n = 1$ and $n > 1$ represent the reflected GO ray field from the ground surface ($n = 1$) and the backscattered GO ray fields from the cylinder objects and small spherical objects in underground volume clusters ($n > 1$), respectively. Finally, the total time-domain GPR signal ($y_{Rx}(t)$) due to all of the propagation channels of the N-channel at each receiver location ($P(x, y, z)$) can be obtained by (3).

B. RAY TRACING TECHNIQUE

In this section, the ray-tracing technique is utilized for calculating the ray paths of each propagation channel, as shown in Fig. 3. The underground target objects are represented by finite length cylinders. The underground random object clusters are represented by small spheres. The GPR electronic equipment is mounted on a drone. Thus, the Tx and Rx antennas are located at the same location and point to the ground (perpendicular to the ground). The ground-reflected ray is always perpendicular to the ground due to the Tx and Rx antenna pointing to the ground. In this case, the incident ($s^i = z$) and reflected GO ray paths from the ground surface ($s^r = z$) are simply calculated. However, the GO ray path of the object underground is more complicated. The GO ray path in the air is calculated by shooting rays from the drone location $P(x,y,z)$ to the unknown searching point on the ground $X_s(x,y,0)$, as shown in Fig. 3.

The ray path underground is calculated from $X_s(x,y,0)$ to the target object location $O_s(x,y,z)$. Snell's law of refraction in (14) is employed in the searching procedure in order to find the refraction point ($X_s(x,y,0)$) of all cylinder target objects and small sphere clusters. The selected study case of the ray paths of the cylinder target objects and underground random object clusters is shown in Fig. 3. Moreover, the total number of rays ($N = 2P_n(M_t + N_s + 1)$) can be calculated by the number of drone locations (P_n) multiplied by the total number of underground cylinder objects (M_t) and small sphere clusters (N_s) and ground reflected ray ($N_g = P_n$). Snell's law is employed to trace the ray in the air and the refracted ray under the ground. Snell's law is written as

$$\frac{\sin(\theta_1)}{\sin(\theta_2)} = \frac{v_1}{v_2} = \frac{n_2}{n_1}. \tag{14}$$

In this study, average soil and sandy wet soil are employed. The soil electrical property is represented by the dielectric constant $\varepsilon_r = \varepsilon'_r - j\varepsilon''_r = \varepsilon'_r - j\sigma/\omega\varepsilon_0$, where σ represents the conductivity (S/m). Additionally, $n = \sqrt{\mu_r\varepsilon_r}$ represents the refraction index. Normally, the σ is very small and $\mu_r = 1$. Thus, the velocity of the GO ray field traveling inside the soil can be determined as

$$v = c/\sqrt{\mu_r\varepsilon_r}. \tag{15}$$

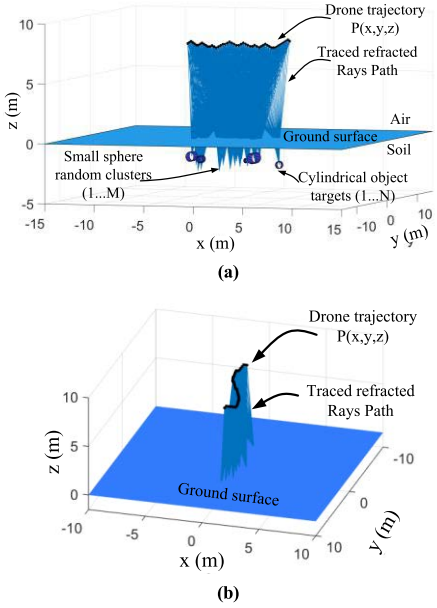

FIGURE 4. (a) The selected case study, the GO ray paths of five cylinder object targets, and small sphere random object clusters of 20 spheres; (b) perspective view of the drone trajectory.

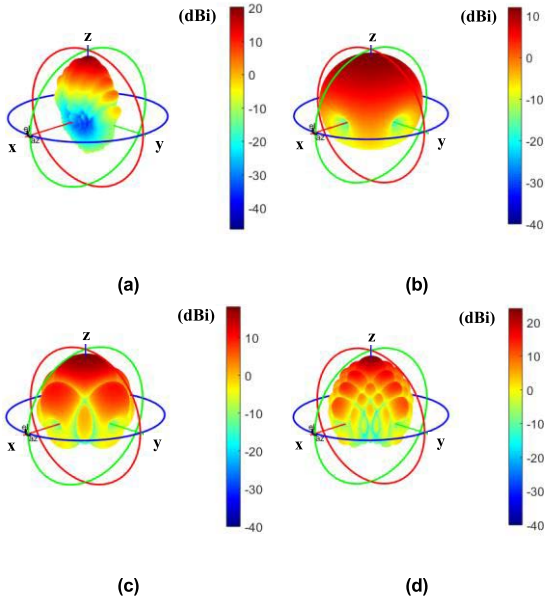

FIGURE 5. Antenna radiation patterns and gain (dBi), (a) imported horn antenna radiation pattern data from the 3D simulation program (HOBBIES), (b) 2 × 2 antenna array, (c) 4 × 4 antenna array (d) 8 × 8 antenna array.

The drone mounted-GPR target distance can be determined by using the signal time delay (t_d) by

$$R = v\frac{t_d}{2}, \tag{16}$$

where $v = c$ for the GO ray field traveling in the air. The selected case study of five cylinder target objects and small sphere random object clusters of 20 spheres, and all of the ray paths and a perspective view of the drone trajectory are illustrated in Fig. 4.

C. ANTENNA RADIATION PATTERN MODELING

The effect of various kinds of antenna radiation patterns on the drone mounted-GPR image can be studied by using the proposed method. 3D radiation pattern data as a function of incoming and outgoing wave angles of $0° \leq \theta \leq 180°$ and $0° \leq \phi \leq 360°$ are required. Tx and Rx antenna radiation patterns can be obtained by using measured data, simulated data from the 3D simulation program such as the CST Microwave Studio [25], or the synthesis of a planar array antenna as shown in Fig. 5. The imported antenna radiation pattern data can be written as

$$F_{ANT.}(\theta, \phi) = Interp.(D(i, k)) \tag{17}$$

where $D(i, k)$ represents the imported pattern data matrix (measurement or simulation) of $i \times k$ with a sampling resolution of 1 degree ($\Delta\Omega = 1°$) or greater, depending upon the accuracy requirement. The 3D interpolation technique for any radiation direction is employed. The radiation pattern of horn antenna with 20 dBi gain from the Higher Order Basis Based Integral Equation Solver (HOBBIES) is imported, as shown in Fig. 5(a). Moreover, the effect of various radiation pattern configurations on the drone mounted-GPR image can be studied by using the planar array synthesis as

$$F_{ANT.}(\theta, \phi) = Interp.(F(\theta, \phi) \cdot AF(\theta, \phi)) \tag{18}$$

where $F(\theta, \phi)$ denotes the pattern data of a single antenna element. $AF(\theta, \phi)$ denotes the planar array factor and can be written as

$$AF(\theta, \phi) = \left\{ \frac{\sin\left(M\frac{\psi_x}{2}\right)}{\sin\left(\frac{\psi_x}{2}\right)} \right\} \left\{ \frac{\sin\left(N\frac{\psi_y}{2}\right)}{\sin\left(\frac{\psi_y}{2}\right)} \right\} \tag{19}$$

where M and N are the number of arrays in x and y directions, respectively. The single antenna element with a unidirectional radiation pattern $F(\theta, \phi) = (1 + \cos(\theta))^2$ is employed. The synthesized array antenna patterns of 2×2 elements, 4×4 elements, and 8×8 elements are shown in Fig. 5(b)-(d), respectively.

D. OBJECT MODELING AND RADAR CROSS SECTION

The σ denotes the RCS in terms of power density. Note that the GO RCS in terms of the EM field is approximately calculated by $\sigma_{Object}^{\text{GO field}} \approx \sqrt{\sigma}$. A gas tank and pipe bomb underground are represented by a finite cylindrical object as shown in Fig. 6. The complex backscattered RCS of the cylinder object [23] can be written as

$$\sigma_{RCS-Cylinder} = \frac{2\pi L^2 a}{(v_2/f)} \tag{20}$$

where L, f and a denote the length of the cylinder, and operating frequency and radius of the cylinder, respectively. However, the cylindrical object configuration is symmetric

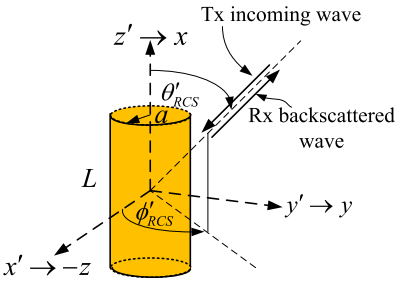

FIGURE 6. Finite length cylindrical object model.

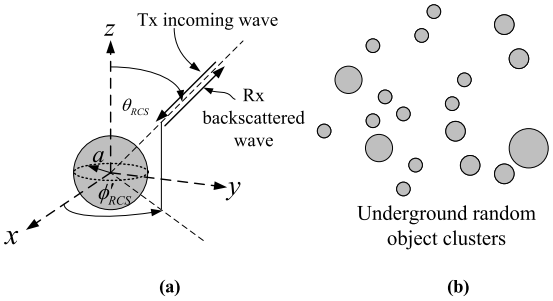

FIGURE 7. (a) Coordinate of sphere object, (b) underground random object clusters are modeled using small spherical objects.

with respect to the axis. Thus, far-field approximation can be applied. Equation (20) can be reduced as

$$\sigma_{RCS-Cylinder} = \frac{a\,(v_2/f)\sin(\theta)}{8\pi\cos^2(\theta)} \tag{21}$$

E. UNDERGROUND RANDOM OBJECT CLUSTERS MODELING

In practical terms, the underground small stone and gravel used to construct the road were therefore represented by the small underground scattered objects, as shown in Fig. 1. Conventionally, the GPR signal loss from the ground can be predicted by small-scale scatter modeling, which is dependent on spatial size radius a, and number per unit volume $N_{obj.}$ [3]. The scattering attenuation factor $\alpha_s = N_{obj.}A/2$. $A = Ca^6f^4$ denotes the Rayleigh scattering cross section, where f and C denote the frequency and constant value, respectively. Scattering attenuation must be added to ohmic loss $\alpha_{total} = \alpha_{ohmic} + \alpha_s$. The cylindrical objects (targets) are embedded a few centimeters under the ground. The number per unit volume $N_{obj.}$ and size a (on top of the targets) will be very small. It should be noted that α_s is very small compared with α_{ohmic} and can be neglected. However, the signal attenuation and fading, namely the underground radar clutter caused by constructive and destructive interference from the multi-path rays of all the small scattered underground objects, are omitted. Therefore, in the proposed work, the Tx and Rx antennas are mounted on a drone. This is considered a far-field scenario. The ohmic or material loss attenuation of a ground and the attenuation caused by the constructive and destructive interference of the small underground scattered objects are taken into account. The backscattered volume clutter radar signals (unwanted signal) from underground are obtained by calculating the backscattered complex RCS of the underground small spherical objects. The RCS of the spherical object from the Mie series [23] can be written as

$$\sigma_{RCS-Sphere} = \left(\frac{j\pi a}{k}\right)\sum_{n=1}^{\infty}(-1)^n(2n-1) \times \left[\frac{kaJ_n(ka) - nJ_n(ka)}{kaH_{n-1}(ka) - nH_n^{(1)}(ka)} - \frac{J_n(ka)}{H_n^{(1)}(ka)}\right] \tag{22}$$

TABLE 1. Summary of target object parameters.

$x(m)$	$y(m)$	$z(m)$	$a(m)$	$L(m)$
-3	-0.8	-0.5	0.15	0.4
-2.5	0	-0.8	0.2	0.6
0.2	1	-1.2	0.1	0.5
2	-0.5	-1	0.2	0.6
2.8	0.6	-0.6	0.25	0.5

where $k = 2\pi/(v_2/f)$ denotes the wave number underneath the ground, and a denotes the radius of the spherical object. $J_n(ka)$ and $H_n^{(1)}(ka)$ denote the Bessel and Hankel functions of order n. However, the high-frequency approximation of the backscattered RCS of the spherical object for a small sphere radius ($r \ll \lambda$) in the Rayleigh region can be written as

$$\sigma_{RCS-Sphere} \approx 9\pi r^2 (kr)^4. \tag{23}$$

For a large sphere radius ($r \gg \lambda$) at the optical region, the normalized complex backscattered RCS of the spherical object can be written as

$$\sigma_{RCS-Sphere} \approx \pi r^2. \tag{24}$$

III. NUMERICAL STUDIES AND RESULTS

In this section, the A-scan and B-scan image of the drone mounted GPR for various study cases will be illustrated. Several target object dimensions and locations are studied, as shown in Table 1. Note that the general 3D drone trajectory can be calculated by using the proposed method. The computational area of $-5 \le x \le 5$m, $-0.5 \le y \le 0.5$m and $-2.1 \le z \le 6$m is employed. The various kinds of soil are shown in Table 2. The Gaussian monopulse in (4) with a signal peak voltage of $V_0 = 1$ volt is employed. The center frequency (f_c) of 1 GHz with a sampling frequency of 8 GHz provides a -3dB bandwidth of 1.16 GHz. Moreover, the effect of center frequency, soil, random object clusters, and the drone location error on the B-scan image of the drone mounted GPR is illustrated.

A. A-SCAN SIGNAL OF A GPR MOUNTED ON A DRONE

The total time-domain receiving signal ($y_{Rx}(t)$) at a fixed location of a drone mounted GPR, normally called an A-scan signal, is plotted, as shown in Fig. 8. The selected case study, the ray tracing of five cylinders with different radii

TABLE 2. Summary of soil parameters [3].

Surface	*Conductivity* σ	*Relative Dielectric Constant* ε_r'
Dry soil	0.001	4-6
Average soil	0.005	16
Sandy wet soil	0.1	25-30

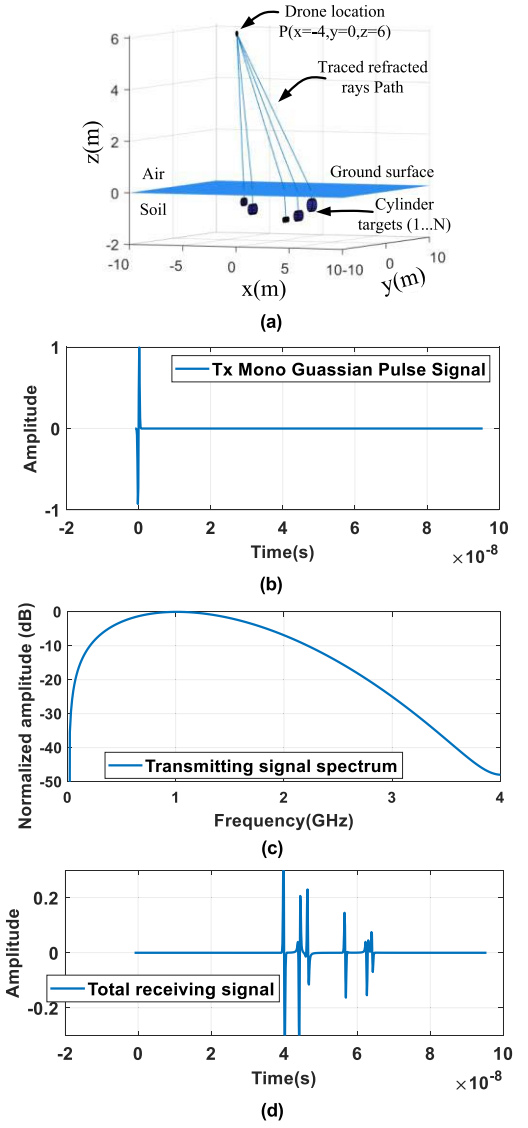

FIGURE 8. The selected case study, (a) ray tracing of five cylinders with different radii and lengths (excluding the reflected ray from the ground) and the drone location of $x = -4$ m, $y = 0$ m, and $z = 6$ m; (b) the Tx Gaussian monopulse signal; (c) center frequency of 1 GHz with a -3dB bandwidth of 1.16 GHz; (d) total receiving A-scan signal of a drone-mounted GPR using a 2 × 2 antenna array radiation pattern, where a computational time of 1.01 seconds is obtained.

and lengths (excluding the reflected ray from the ground), and the drone locations of $x = -4$ m, $y = 0$ m, and $z = 6$ m are illustrated in Fig. 8 (a). Average soil with a conductivity of 0.005 S/m and a relative dielectric constant of $\varepsilon_r = 16$ is employed. The proposed GUI display consists of the drone mounted-GPR location, the GO ray paths, and the

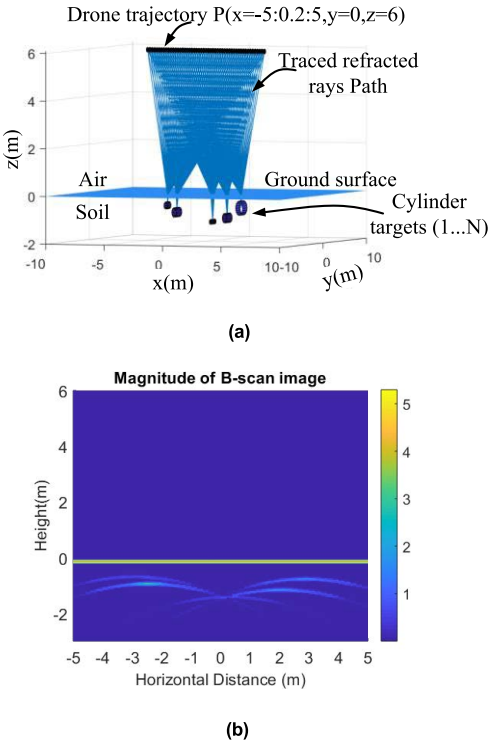

FIGURE 9. The selected case study, B-scan image of a drone mounted GPR of five cylinder objects with different radii (a) and lengths (L) and average soil of $\varepsilon_r = 16$, $\sigma = 0.005$S/m (a) refracted GO ray path (the reflected rays from the ground are not shown) (b) total receiving B-scan image of a drone mounted GPR in the case of horn antennas, the computational time of 1.7 seconds is obtained.

target objects. The Tx Gaussian monopulse signal is shown in Fig. 8 (b). The center frequency of 1 GHz with a -3dB bandwidth of 1.16 GHz is employed, as shown in Fig. 8 (c). Finally, the total receiving A-scan signal of a drone-mounted GPR using a 2 × 2 array antenna radiation pattern is shown in Fig. 8 (d), including the reflected pulse from the ground surface, and the rest of the pulses coming from objects at different locations. The computational time of 1.01 seconds is obtained.

B. B-SCAN IMAGE OF A GPR MOUNTED ON DRONE

The B-scan image of drone mounted GPR is performed by varying the drone trajectory. In the selected case study, the drone locations of $-5 \leq x \leq 5$m with a fixed location of $y = 0$m and an altitude of $z = 6$m are chosen in order to avoid the effect of explosion of the buried IED. Note that the horizontal distance varies from -5 m to 5 m with a resolution of 0.2 m. The total sampling points of 51 points are employed. The GO ray paths of five cylinders with different radii and lengths (excluding the reflected ray from the ground) and drone trajectory are illustrated in Fig. 9 (a). Average soil with a conductivity of 0.005 S/m and a relative dielectric constant of $\varepsilon_r = 16$ is employed. The total receiving B-scan image in the case of the imported horn antenna radiation pattern is illustrated in Fig. 9 (b). The antenna gain of 20 dBi is employed as shown in Fig. 5 (a). It is found that the hyperbolic

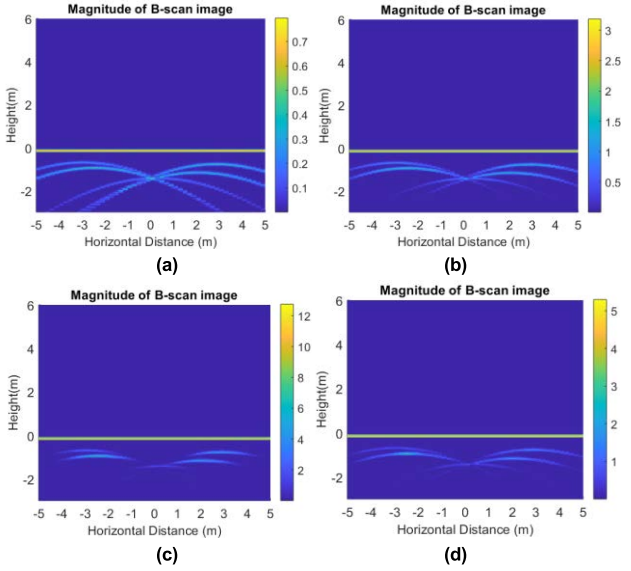

FIGURE 10. The selected case study, B-scan image of a drone mounted GPR of five cylinder objects and average soil of $\varepsilon_r = 16$, $\sigma = 0.05$S/m, (a) Synthesized 2 × 2 array antenna radiation pattern, (b) 4 × 4 array antenna radiation pattern, (c) 8 × 8 array antenna radiation pattern (d) Imported horn antenna radiation pattern in the case of a wide beamwidth xz-plane radiation pattern, the computational time is less than two seconds.

signature of the objects underneath the ground in the B-scan image can be detected. The location of the objects underneath the ground is illustrated and the computational time of 1.7 seconds is obtained.

C. EFFECT OF THE ANTENNA RADIATION PATTERN ON THE GPR B-SCAN IMAGE

The effect of the antenna radiation pattern on the GPR B-scan image is studied. The synthesized 2 × 2 array with the half power beamwidth of 66.0 degrees and a gain of 12 dBi, a 6 × 6 array with the half power beamwidth of 22.0 degrees and a gain of 21.5 dBi, a 8 × 8 array with the half power beamwidth of 18.0 degrees and a gain of 24.0 dBi, and imported horn antenna radiation patterns with the half power beamwidth of 16.0 degrees and a gain of 20.0 dBi are employed, as shown in Fig. 5. It is found that the hyperbolic signature of the objects underneath the ground in the B-scan image depends on the antenna radiation pattern. The high gain and narrow HPBW antenna pattern provide a high signal magnitude and narrow hyperbolic signature, as shown in Fig. 10. The computational time is less than 2 seconds.

D. EFFECT OF CENTER FREQUENCY ON THE GPR B-SCAN IMAGE

In the selected case study, the B-scan image of a drone mounted GPR of five cylinder objects and average soil of $\varepsilon_r = 16$, $\sigma = 0.05$ S/m is calculated as shown in Fig.11. The drone trajectory of $-5 \le x \le 5$ m with a fixed location of $y = 0$ m and an altitude $z = 6$ m is selected. The Gaussian monopulse in (4) with a $V_0 = 1$ volt signal peak voltage is employed. The center frequency (f_c) of 1 GHz and

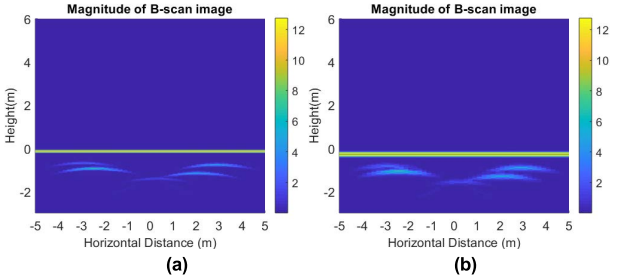

FIGURE 11. Effect of the center frequency of the drone mounted GPR on the B-scan image (× array antenna radiation pattern and without volume cluster) (a) $f_c = 1$ GHz, (b) $f_c = 0.5$ GHz, the computational time is less than two seconds.

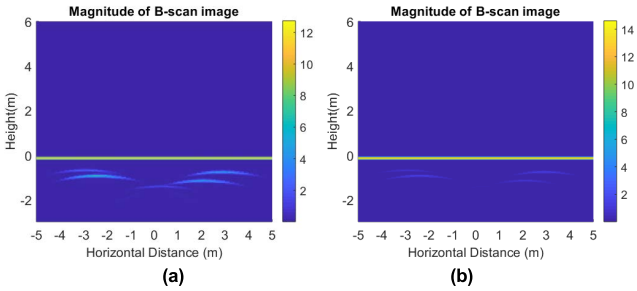

FIGURE 12. Total receiving signal B-scan image of a drone mounted GPR using an 8 × 8 array antenna, (a) average soil with $\varepsilon_r = 16$ and $\sigma = 0.05$S/m, (b) sandy wet soil with $\varepsilon_r = 30$ and $\sigma = 0.1$S/m.

0.5 GHz with a sampling frequency (f_s) of 8 GHz is employed. First, the center frequency (f_c) of 0.5 GHz provides a -3dB bandwidth of 0.6 GHz. Secondly, the center frequency (f_c) of 1 GHz provides a -3dB bandwidth of 1.16 GHz. It is seen that the resolution of the hyperbolic signature in the B-scan image depends on the center frequency (f_c) and the -3dB bandwidth, as shown in Fig.11. The large -3dB bandwidth provides more resolution of the hyperbolic signature.

E. EFFECT OF GROUND TYPES ON THE GPR B-SCAN IMAGE

The various kinds of soil are shown in Table 2. As indicated, in this study, average soil and sandy wet soil are employed. The soil electrical property is represented by the dielectric constant $\varepsilon_r = \varepsilon_r' - j\varepsilon_r'' = \varepsilon_r' - j\sigma/\omega\varepsilon_0$ where σ represents the conductivity (S/m). The total receiving signal B-scan image of a drone mounted GPR using an 8 × 8 array antenna radiation pattern is shown in Fig. 12. The calculated results of average soil and sandy wet soil cases with $\varepsilon_r = 16$ and $\sigma = 0.005$ S/m, and $\varepsilon_r = 30$ and $\sigma = 0.1$ S/m are shown in Fig. 12 (a) and Fig. 12 (b), respectively. The sandy wet soil provides more reflection by the ground surface and the magnitude of the hyperbolic signature is very low.

F. EFFECT OF UNDERGROUND RADAR VOLUME CLUTTER

The underground radar volume clutter is an unwanted signal, generated by unknown, underground objects. These objects are represented by random small spherical objects. The position (x,y,z) and dimension are randomly created.

TABLE 3. Computational time of selected study cases.

Study Cases	*No.of Cyl.*	*No. of Small Sph. in Volume Cluster*	*No. of GO Rays*	*Computational Time*, Average soil* ($\varepsilon_r = 16$, $\sigma = 0.005$ *S/m*)
1	5	-	256	<2 seconds
2	5	500	25,756	~11 minutes
3	5	2,000	102,256	~47 minutes
4	5	4,000	204,256	~96 minutes
5	5	6,000	306,256	~157 minutes

Note that the horizontal distance varies from -5 m to 5 m with a resolution of 0.2 m. The total sampling points are 51 points. A laptop computer, using Intel i7-8565U, and a 1.8 GHz clock speed with 24 GB RAM, is employed. *Computational time depends on the computer performance.

The random object clusters are located in the considered underground area of $10 \times 1 \times 2$ m^2 ($-5 \leq x \leq 5$ m, $-0.5 \leq y \leq 0.5$ m and $-2.1 \leq z \leq -0.1$ m). The radii of small spherical objects of $1 \leq a \leq 6$ cm is employed in the random process with the number of small spheres of 500 spheres (25 points per m^3), 2,000 spheres (100 points per m^3), 4,000 spheres (200 points per m^3), and 6,000 spheres (300 points per m^3). The RCS of each small spherical object is calculated using (22)-(24). The GO ray paths, free-space path-loss, underground path-loss, and phase delay due to each GO ray path propagation channels are calculated. The calculated results of average soil with $\varepsilon_r = 16$ and $\sigma = 0.005$ S/m are shown in Fig. 13 (b)-(e). It is found that the random object cluster density affects the B-scan image of a drone mounted GPR. The image noise increases due to the increase in the random object cluster density. In the case of 4,000 random spheres and 6,000 random spheres, some of the hyperbolic signatures of the underground cylinder objects disappeared. The total computational time of the selected study cases is shown in Table 3. The proposed method is very efficient.

G. EFFECT OF DRONE ALTITUDE ERROR

The drone mounted-GPR altitude errors that resulted from the drone hovering are preliminarily studied in this section by using the proposed simulation method. Since the proposed simulation procedure supports the 3D complex scenario, the x and y position errors can be included. Practically, x and y position errors can be reduced by using high-accuracy GPS and high-accuracy data acquisition. The drone mounted-GPR signal will be collected at the correct position. The scenario modeling is the same as in Section III (E) and (F). The 4,000 random spheres with a radius of $1 \leq a \leq 6$ cm (200 spheres per m^3) are randomly embedded into the ground to represent the underground random object clusters, which are located at the considered underground area of $-5 \leq x \leq 5$ m, $-0.5 \leq y \leq 0.5$ m, and $-2 \leq z \leq 0$ m ($10 \times 1 \times 2$ m^3). The drone mounted-GPR altitude is fixed at 6 m. However, altitude error between 5.5 m and 6.2 m was randomly generated. It was found that the drone-mounted GPR altitude error affects the hyperbolic signature in the B-scan GPR image, as shown in Fig. 14. In the case of not having random

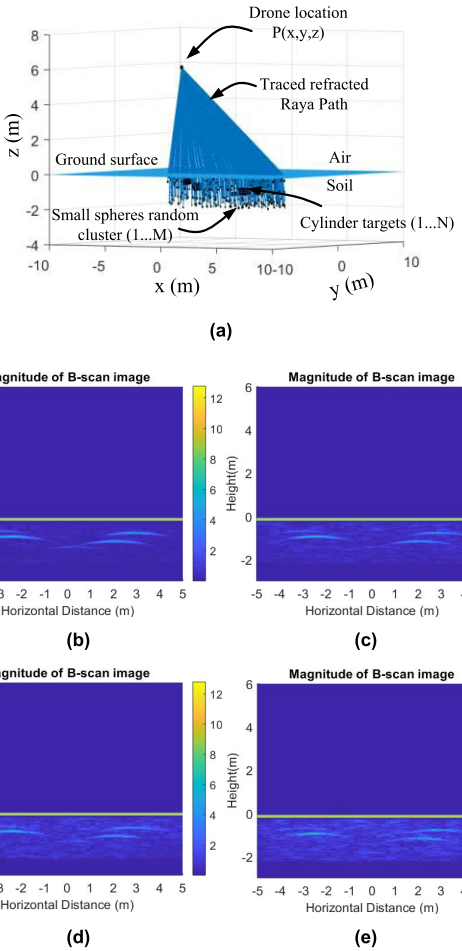

FIGURE 13. Total receiving signal B-scan image of a drone mounted GPR of five cylinder objects, average soil ($\varepsilon_r = 16$, $\sigma = 0.005$ S/m) and 8 × 8 array antenna radiation pattern with random object clusters (small sphere radii of 1 cm to 6 cm), (a) GO ray paths, (b) 500 spheres (25 points per m^3), (c) 2,000 spheres (100 points per m^3), (d) 4,000 spheres (200 points per m^3), (e) 6,000 spheres (300 points per m^3), the computational times are 11 min, 47 min, and 96 min and 157 min, respectively.

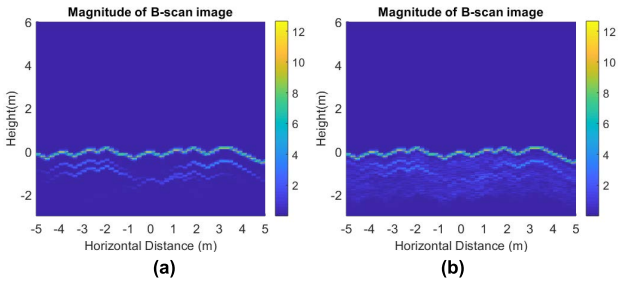

FIGURE 14. Effect of drone-mounted GPR altitude error on the B-scan image using an × array antenna, (a) without random object clusters with a computational time of two seconds, and (b) included random object clusters with a computational time of 92 minutes.

object clusters, as shown in Fig. 14 (a), the hyperbolic signatures of the underground cylinder objects are distorted. However, the underground cylinder object signatures still

appear in the B-scan image. Thus, the post processing of object recognition and drone mounted-GPR altitude error compensation techniques is required. Moreover, in the case of the 4,000 underground random object clusters, they are shown in Fig. 14 (b). The image noise increases due to the increase in the random object cluster density. Unfortunately, the hyperbolic signatures of the underground cylinder objects are totally distorted and cannot be detected. It is directly dependent on the density of the underground random object clusters. In this situation, the B-scan image noise reduction technique is required.

IV. CONCLUSION

The proposed simulation method can predict drone mounted-GPR signals in the complex 3D scenario, including the reflected signal from various ground types, backscattered signals from the considered underground objects, and backscattered volume clutter signals from the random object clusters underneath the ground. Moreover, the effect of drone position errors and antenna radiation patterns on the A-scan and B-scan images of a drone mounted GPR can be calculated. It is found that the hyperbolic signature intensity of the target objects underneath the ground depends on the antenna radiation pattern, the density of the random object clusters, ground types, and the drone position error. The proposed simulation method is useful for studying drone mounted-GPR signals in complex 3D scenarios, various kinds of transmitting signals, and target object configurations and antennas. Especially, the proposed simulation method can be useful for the investigation of several post processing hyperbolic signature recognition algorithms and image noise reduction techniques as well. Moreover, a signal processing technique employed to retrieve the parabola damaged from the altitude error of the drone mounted GPR can be presented in future publication.

REFERENCES

[1] A. Benedetto, F. Tosti, L. B. Ciampoli, and F. D'Amico, "GPR applications across engineering and geosciences disciplines in Italy: A review," *IEEE J. Sel. Topics Appl. Earth Observ. Remote Sens.*, vol. 9, no. 7, pp. 2952–2965, Jul. 2016, doi: 10.1109/JSTARS.2016.2554106.

[2] A. Benedetto and L. Pajewski, *Civil Engineering Applications of Ground Penetrating Radar* (Springer Transactions in Civil and Environmental Engineering). Berlin, Germany: Springer, 2015.

[3] H. M. Jol, *Ground Penetrating Radar Theory and Applications*. Amsterdam, The Netherlands: Elsevier, 2009, pp. 15–18, doi: 10.1016/B978-0-444-53348-7.00018-1.

[4] A. Boonpoonga, "Ground penetrating radar (GPR) for counter improvised-explosive devices in Thailand," in *Proc. IEEE Conf. Antenna Meas. Appl. (CAMA)*, Nov. 2015, pp. 1–3, doi: 10.1109/CAMA.2015.7428148.

[5] N. Chantasen, A. Boonpoonga, S. Burintramart, K. Athikulwongse, and P. Akkaraekthalin, "Automatic detection and classification of buried objects using ground-penetrating radar for counter-improvised explosive devices," *Radio Sci.*, vol. 53, no. 2, pp. 210–227, Feb. 2018, doi: 10.1002/2017RS006402.

[6] M. Schutz, C. Decroze, M. Lalande, and B. Lenoir, "Design study for UAV-mounted GPR," in *Proc. 49th Eur. Microw. Conf. (EuMC)*, Oct. 2019, pp. 333–336.

[7] M. G. Fernàndez, Y. A. López, A. D. Mitri, D. C. Martínez, G. A. Narciandi, and F. L. Andrés, "Portable and easily-deployable air-launched GPR scanner," *Remote Sens.*, vol. 12, no. 11, p. 1833, 2020.

[8] M. G. Fernández, Y. Á. López, B. G. Valdés, Y. R. Vagueiro, F. L. Andrés, and A. P. García, "Synthetic aperture radar imaging system for landmine detection using a ground penetrating radar on board a unmanned aerial vehicle," *IEEE Access*, vol. 6, pp. 45100–45112, 2018, doi: 10.1109/ACCESS.2018.2863572.

[9] M. García-Fernández, Y. Á. López, and F. L.-H. Andrés, "Airborne multi-channel ground penetrating radar for improvised explosive devices and landmine detection," *IEEE Access*, vol. 8, pp. 165927–165943, 2020, doi: 10.1109/ACCESS.2020.3022624.

[10] J. Colorado, C. Devia, M. Perez, I. Mondragon, D. Mendez, and C. Parra, "Low-altitude autonomous drone navigation for landmine detection purposes," in *Proc. Int. Conf. Unmanned Aircr. Syst. (ICUAS)*, 2017, pp. 540–546, doi: 10.1109/ICUAS.2017.7991303.

[11] R. M. Beauchamp, D. D. Arumugam, and M. S. Burgin, "Can airborne ground penetrating radars explore groundwater in hyper-arid regions?" *IEEE Access*, vol. 6, pp. 27736–27759, 2018, doi: 10.1109/ACCESS.2018.2840038.

[12] P. D. Walker and M. R. Bell, "Noniterative techniques for GPR imaging through a nonplanar air-ground interface," *IEEE Trans. Geosci. Remote Sens.*, vol. 40, no. 10, pp. 2213–2223, Oct. 2002, doi: 10.1109/TGRS.2002.802458.

[13] P. Pathak, W. Burnside, and R. Marhefka, "A uniform GTD analysis of the diffraction of electromagnetic waves by a smooth convex surface," *IEEE Trans. Antennas Propag.*, vol. AP-28, no. 5, pp. 631–642, Sep. 1980, doi: 10.1109/TAP.1980.1142396.

[14] P. Pathak, "High frequency techniques for antenna analysis," *Proc. IEEE*, vol. 80, no. 1, pp. 44–65, Jan. 1992, doi: 10.1109/5.119566.

[15] K. Phaebua, C. Phongcharoenpanich, M. Krairiksh, and T. Lertwiriyaprapa, "Path-loss prediction of radio wave propagation in an orchard by using modified UTD method," *Prog. Electromagn. Res.*, vol. 128, pp. 347–363, 2012, doi: 10.2528/PIER12040106.

[16] M. Sarestoniemi, M. Hamalainen, and J. Iinatti, "An overview of the electromagnetic simulation-based channel modeling techniques for wireless body area network applications," *IEEE Access*, vol. 5, pp. 10622–10632, 2017, doi: 10.1109/ACCESS.2017.2708161.

[17] S. Niu, X. Qiu, B. Lei, and K. Fu, "A SAR target image simulation method with DNN embedded to calculate electromagnetic reflection," *IEEE J. Sel. Topics Appl. Earth Observ. Remote Sens.*, vol. 14, pp. 2593–2610, 2021, doi: 10.1109/JSTARS.2021.3056920.

[18] C. Ozdemir, S. Demirci, E. Yigit, and A. Kavak, "A hyperbolic summation method to focus B-scan ground penetrating radar images: An experimental study with a stepped frequency system," *Microw. Opt. Technol. Lett.*, vol. 49, no. 3, pp. 671–676, Mar. 2007.

[19] K. Phaebua, A. Boonpoonga, and S. Burintramart, "Time-domain GPR signal prediction by using time-domain UTD method," in *Proc. 17th Int. Conf. Electr. Eng., Electron., Comput., Telecommun. Inf. Technol. (ECTI-CON)*, 2020, pp. 836–839, doi: 10.1109/ECTI-CON49241.2020.9158252.

[20] K. Phaebua, T. Lertwiriyaprapa, A. Boonpoonga, and S. Burintramart, "Signal prediction of a GPR system mounted on drone by using ray-tracing technique," in *Proc. 9th Int. Electr. Eng. Congr. (IEECON)*, 2021, pp. 539–542, doi: 10.1109/iEECON51072.2021.9440372.

[21] T. Yamaguchi, T. Mizutani, K. Meguro, and T. Hirano, "Detecting subsurface voids from GPR images by 3-D convolutional neural network using 2-D finite difference time domain method," *IEEE J. Sel. Topics Appl. Earth Observ. Remote Sens.*, vol. 15, pp. 3061–3073, 2022, doi: 10.1109/JSTARS.2022.3165660.

[22] S. Eide, T. Casademont, O. L. Aardal, and S.-E. Hamran, "Modeling FMCW radar for subsurface analysis," *IEEE J. Sel. Topics Appl. Earth Observ. Remote Sens.*, vol. 15, pp. 2998–3007, 2022, doi: 10.1109/JSTARS.2022.3165135.

[23] B. R. Mahafza, *Radar Systems Analysis and Design Using MATLAB*. Oxfordshire, U.K.: Taylor & Francis, 2005.

[24] A. C. Balanis, *Advanced Engineering Electromagnetics*. New York, NY, USA: Wiley, 1989.

[25] *CST Studio Suite (User's Manual)*, 3DS Dassault Syst., Tokyo, Japan, 2019.

[26] V. Zhurbenko, Ed., *Electromagnetic Waves*. London, U.K.: IntechOpen, 2011. [Online]. Available: https://www.intechopen.com/books/166, doi: 10.5772/693.

[27] H. Lawrence, "Modelling the effects of surface roughness and a forest litter layer on passive microwave observations: Application to soil moisture retrieval by the SMOS mission," Continental Interfaces, Environ., Université Sci. et Technol., Bordeaux, France, Tech. Rep. tel-01024075, 2010. [Online]. Available: https://tel.archives-ouvertes.fr/tel-01024075

KITTISAK PHAEBUA (Member, IEEE) received the B.Eng. and M.Eng. degrees in telecommunication engineering and the Ph.D. (Eng.) degree in electrical engineering from the King Mongkut's Institute of Technology Ladkrabang (KMITL), Bangkok, Thailand, in 2006, 2008, and 2012, respectively. He is currently an Assistant Professor with the Department of Teacher Training in Electrical Engineering, King Mongkut's University of Technology North Bangkok, Thailand. His research interests include the computation of electromagnetic using high frequency techniques and antenna and microwave filter design for wireless communication systems.

TITIPONG LERTWIRIYAPRAPA (Senior Member, IEEE) received the B.S.Tech.Ed. degree in electrical engineering from the King Mongkut's University of Technology North Bangkok, in 1996, the M.Eng. degree in electrical engineering from the King Mongkut's Institute of Technology Ladkrabang, in 2000, and the M.Sc. and Ph.D. degrees in electrical engineering from The Ohio State University, Columbus, OH, USA, in 2006 and 2007, respectively. He is currently an Associate Professor with the Department of Teacher Training in Electrical Engineering, King Mongkut's University of Technology North Bangkok. His research interests include electromagnetic theory, metamaterial, asymptotic, computational electromagnetics, and hybrid methods. He has received the Third Place in the 2007 USNCCNC URSI Student Paper Competition, held in Ottawa, Canada, and the Best Paper Award in the 2008 International Symposium on Antennas and Propagation (ISAP2008), held in Taiwan. He serves as a board of the ECTI Association, from 2012 to 2015 and from 2020 to 2023.

SANTANA BURINTRAMART received the B.S. degree in electrical engineering from the Chulachomklao Royal Military Academy, Thailand, in 1998, and the M.S. and Ph.D. degrees in electrical engineering from Syracuse University, NY, USA, in 2004 and 2009, respectively. He has worked as the Director of the Explosive Engineering Division, Defence Technology Institute (DTI), Thailand, during 2016–2019. He currently works at his private company, which provides consultation on technology development and intellectual property protection.

AKKARAT BOONPOONGA (Member, IEEE) received the B.Eng. degree in electrical engineering from the King Mongkut's University of Technology North Bangkok (KMUTNB), Bangkok, Thailand, in 2002, and the M.Eng. degree in telecommunications engineering and the D.Eng. degree in electrical engineering from the King Mongkut's Institute of Technology Ladkrabang (KMITL), Bangkok, in 2004 and 2008, respectively. He is currently an Associate Professor with the Department of Electrical and Computer Engineering, Faculty of Engineering, KMUTNB. His research interests include ground-penetrating radar (GPR), radar systems, radar target identification, the chipless RFID systems, and signal processing for EM applications. He is a member of the ECTI Association, Thailand. He was a Board Committee Member of the ECTI Association, from 2016 to 2017 and from 2020 to 2021.